



Ductile machining of single-crystal silicon for microlens arrays by ultraprecision diamond turning using a slow tool servo



Mao Mukaida, Jiwang Yan*

Department of Mechanical Engineering, Faculty of Science and Technology, Keio University, 3-14-1 Hiyoshi, Kohoku-ku, Yokohama 223-8522, Japan

ARTICLE INFO

Keywords:

Single-crystal silicon
Ultraprecision cutting
Diamond turning
Slow tool servo
Microlens array
Infrared optics

ABSTRACT

Microlens arrays of single-crystal silicon are required increasingly in advanced IR optics. In this study, we attempted to machine spherical concave microlens arrays on a single-crystal silicon wafer by slow tool servo diamond turning. The form error, surface topography, material phase transformation, and cutting force characteristics were investigated experimentally. It was found that brittle fracture occurred preferentially at one side (the exit side of tool feed) of the lens dimples when cutting direction is along $\langle 110 \rangle$ and tool feed rate is high. Amorphous silicon phase was generated significantly at one side (the exit side of tool feed) of the dimples as tool feed rate increased. The peak values and the direction angles of cutting forces changed with tool feed rate, crystal orientation, and the cutting direction. Two kinds of tool wear, namely, micro chippings and flank wear were observed in different regions of the tool edge where undeformed chip thickness is different. Spherical microlens arrays with a form error of ~ 300 nmPV and surface roughness of ~ 6 nmSa were successfully fabricated.

1. Introduction

Single-crystal silicon has become increasingly important, not only because of its properties as a semiconductor, but also due to its excellent optical performance in the infrared (IR) region. IR optical systems are used in a wide range of applications such as night vision systems, dark-field devices, and so on. Single-crystal silicon has been used as an IR optical material in flat, spherical or aspherical shapes [1–4]. Recently, advanced optical systems require optical elements having more complex shapes, such as freeform optics, to improve optical performance and/or to create new functions. For example, microlens arrays are used in advanced high-integration and high-performance optical systems, enabling many kinds of functions. There are two kinds of microlens arrays, namely, concave and convex. Concave microlens arrays work as homogenizers [5–7], optical scanners [8], and so on. They are sometimes combined with convex microlens arrays to enhance optical characteristics, such as view angle and image depth, in imaging systems [9,10]. Convex microlens arrays are widely used in image sensors to focus incident light on photodiodes and to increase the brightness for liquid crystal displays, and in Shack-Hartmann sensors to measure wavefront aberrations [11–14]. Up to date, most microlens arrays are made of glass and plastics for visible light, whereas the literature on silicon lens arrays for the IR range is very limited.

A few methods have been proposed for machining microlens arrays on silicon, and most of these methods are composed of lithographic processes involving chemical etching [5,6,12,13,15,16]. To enhance the etching process, some researchers proposed laser assisted etching [5,16]. However, the geometries possible to be generated by etching processes are very limited, and it is difficult to ensure the lens surface quality and form accuracy.

In this study, we attempt to machine silicon microlens arrays by ultraprecision cutting, namely, diamond turning, which can produce higher geometric freedom and lower surface roughness than etching. Silicon is a highly brittle material, thus conventionally, grinding and polishing have been used for silicon machining with optical surfaces thus far. However, grinding and polishing are difficult to produce complex surface structures such as microlens arrays. As an alternative approach, ductile cutting of silicon has been extensively investigated [17–24]. However, much of the previous research on the ductile cutting of silicon was performed on flat wafers or spherical/aspherical surfaces, while there is little research on the diamond turning of silicon for microlens arrays.

We aim at generating micro dimples on a silicon substrate which can be used as concave microlens arrays for IR light. Another possible use of micro dimple arrays on silicon is as a mold substrate for molding convex microlens arrays on polymer [11–13]. It has been demonstrated that silicon is useable as a mold substrate material for press

* Corresponding author.

E-mail address: yan@mech.keio.ac.jp (J. Yan).

<http://dx.doi.org/10.1016/j.ijmactools.2016.11.004>

Received 4 July 2016; Received in revised form 12 November 2016; Accepted 19 November 2016

Available online 27 November 2016

0890-6955/ © 2016 Elsevier Ltd. All rights reserved.

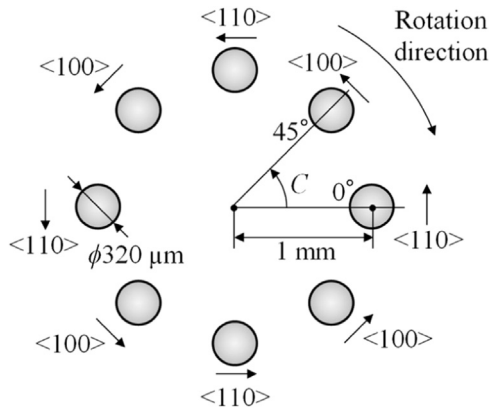


Fig. 1. Schematic of lens dimple shape and crystal orientations of cutting directions.

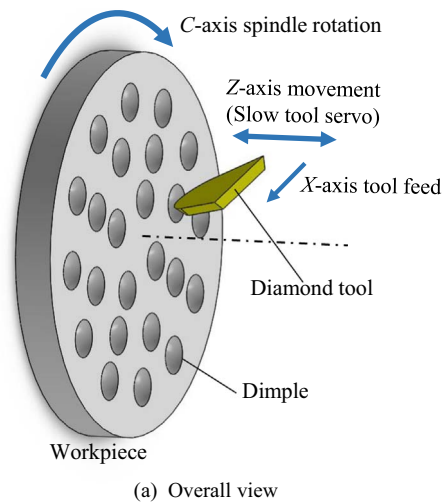


Fig. 2. Schematic of STS diamond turning of a concave microlens array.

molding of glass micro optics [14]. In addition, silicon micro dimple arrays are possible to be used as micro mirrors [15].

A microlens array can be diamond turned by using a tool servo system, such as a slow tool servo (STS) or a fast tool servo (FTS) [25–31], where the tool feeding is synchronized with the spindle rotation.

Table 1
Cutting conditions for microlens arrays of single-crystal silicon.

| Cutting parameters | Values |
|--|------------------------|
| Feed rate f ($\mu\text{m}/\text{rev}$) | 1–6 |
| Depth of cut A_p (μm) | 0–5 |
| Spindle rotation rate N (rpm) | 33–54 |
| Cutting speed V_c (mm/s) | 4.5 |
| Cutting tool | |
| Tool material | Single-crystal diamond |
| Nose radius (mm) | 1.0 |
| Rake angle ($^\circ$) | –30 |
| Relief angle ($^\circ$) | 36 |
| Cutting atmosphere | Dry |

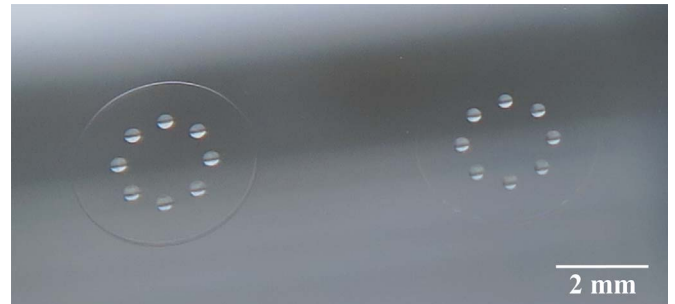


Fig. 3. Photograph of ductile-cut microlens arrays on a silicon wafer.

Compared with other methods, such as micro milling and fly cutting, diamond turning using a tool servo can reduce machining time and thermal expansion/contraction of a workpiece due to changes in surrounding temperature. The main difference between STS and FTS diamond turning is the possible tool servo stroke and reciprocating frequency. FTS diamond turning requires an additional servo unit for tool drive, while in STS diamond turning the tool is driven by Z-axis stage of the machine tool itself. In this study, we attempt to use STS diamond turning to fabricate concave microlens arrays on single-crystal silicon by ductile cutting.

Unlike in conventional diamond turning, the tool posture and cutting point of the tool, as well as the depth of cut change rapidly in STS diamond turning. Thus, the machining mechanism of a highly brittle material, such as MgF_2 glass, becomes very complicated [32]. In this paper, the material removal behavior of silicon, including brittle fracture and phase transformation, cutting force, and tool wear during micro dimple cutting on single-crystal silicon were investigated. The form accuracy and surface topography of the microlens array were evaluated. The objective of this research is to realize micro dimple cutting of silicon in a completely ductile mode, which can be used for fabricating freeform and micro-structured optical surface on single-crystal silicon and other brittle materials.

2. Experimental procedures

As test cuts, spherical micro dimples were machined on a p-type single-crystal silicon (001) wafer. The shape and crystal orientation of the lens dimples on the workpiece are schematically shown in Fig. 1. Each dimple has a designed diameter of $320 \mu\text{m}$ and a curvature radius (R_d) of 2.563 mm , thus the depth of the dimple (D) is $5 \mu\text{m}$. The dimples are located 1 mm away from the workpiece center, at an angular pitch of 45° . The cutting directions for the dimples located at $C=0^\circ, 90^\circ, 180^\circ, 270^\circ$ are $\langle 110 \rangle$ directions, while those at $C=45^\circ, 135^\circ, 225^\circ, 315^\circ$ are $\langle 100 \rangle$ directions.

A four-axis (XZBC) simultaneous control ultraprecision lathe Nanoform X (AMETEK Precitech Inc., USA) having an STS system was used in the experiments. Machining principles of STS diamond turning of micro dimples is shown in Fig. 2. The tool paths were

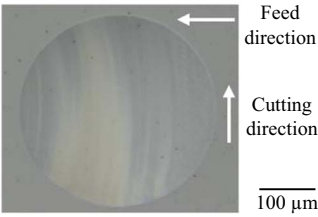
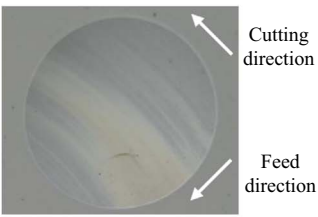
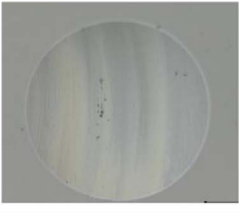
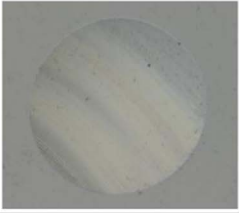
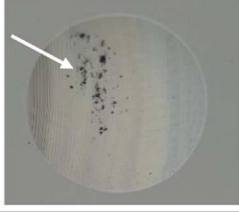
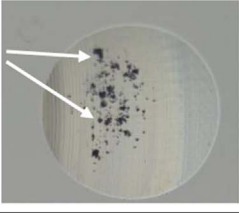
| f ($\mu\text{m}/\text{rev}$) | $C = 0^\circ$ Cutting direction $\langle 110 \rangle$ | $C = 45^\circ$ Cutting direction $\langle 100 \rangle$ |
|-------------------------------------|---|--|
| 1 |  |  |
| 2 |  |  |
| 3 |  |  |
| 4 |  |  |
| 5 |  |  |
| 6 |  |  |

Fig. 4. Microscopic images of dimples machined at various tool feed rates along different cutting directions.

generated using the CAM software DIFFSYS. A single-crystal diamond tool with a nose radius (R_n) of 1 mm, a rake angle of -30° , and a relief angle of 36° was used.

Experimental conditions are summarized in Table 1. All experiments were conducted under dry condition in order to collect cutting chips. The workpiece spindle rotated clockwise and its rotation rate was changed automatically during cutting so that the cutting speed remained constant in all the cutting areas. Cutting experiments were conducted under various feed rates f to investigate the effect of undeformed chip thickness.

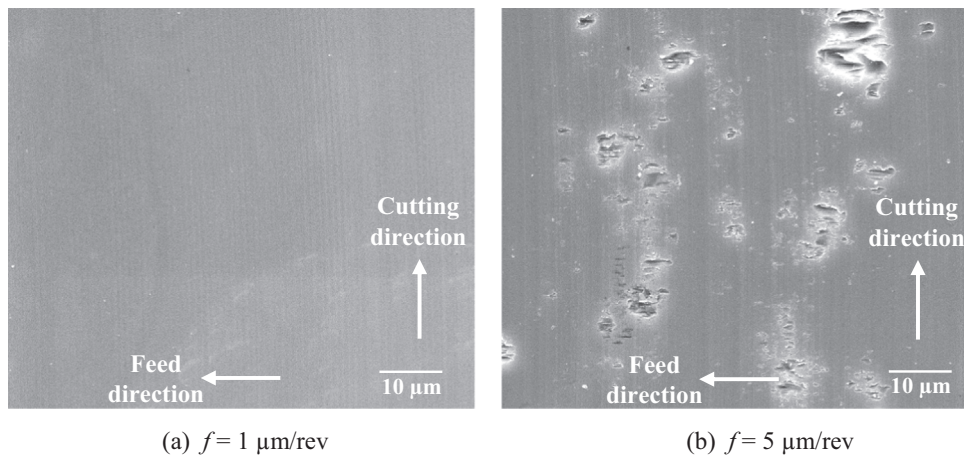
Cutting forces were measured using a piezoelectric dynamometer Kistler 9256C2. The machined dimple surfaces were observed using a

digital microscope and a scanning electron microscope (SEM). Three-dimensional topographies of the dimples were measured using a white light interferometer Talysurf CCI1000 (AMETEK Taylor Hobson Ltd., UK). A laser micro-Raman spectrometer (JASCO NRS-3100, Japan) was used to examine phase transformation of silicon caused by machining.

3. Results and discussion

3.1. Ductile-brittle transition

Fig. 3 shows a photograph of microlens arrays machined on a



(a) $f = 1 \mu\text{m/rev}$ (b) $f = 5 \mu\text{m/rev}$

Fig. 5. SEM images of dimple surfaces located at $C=0^\circ$ cut at different tool feed rates.

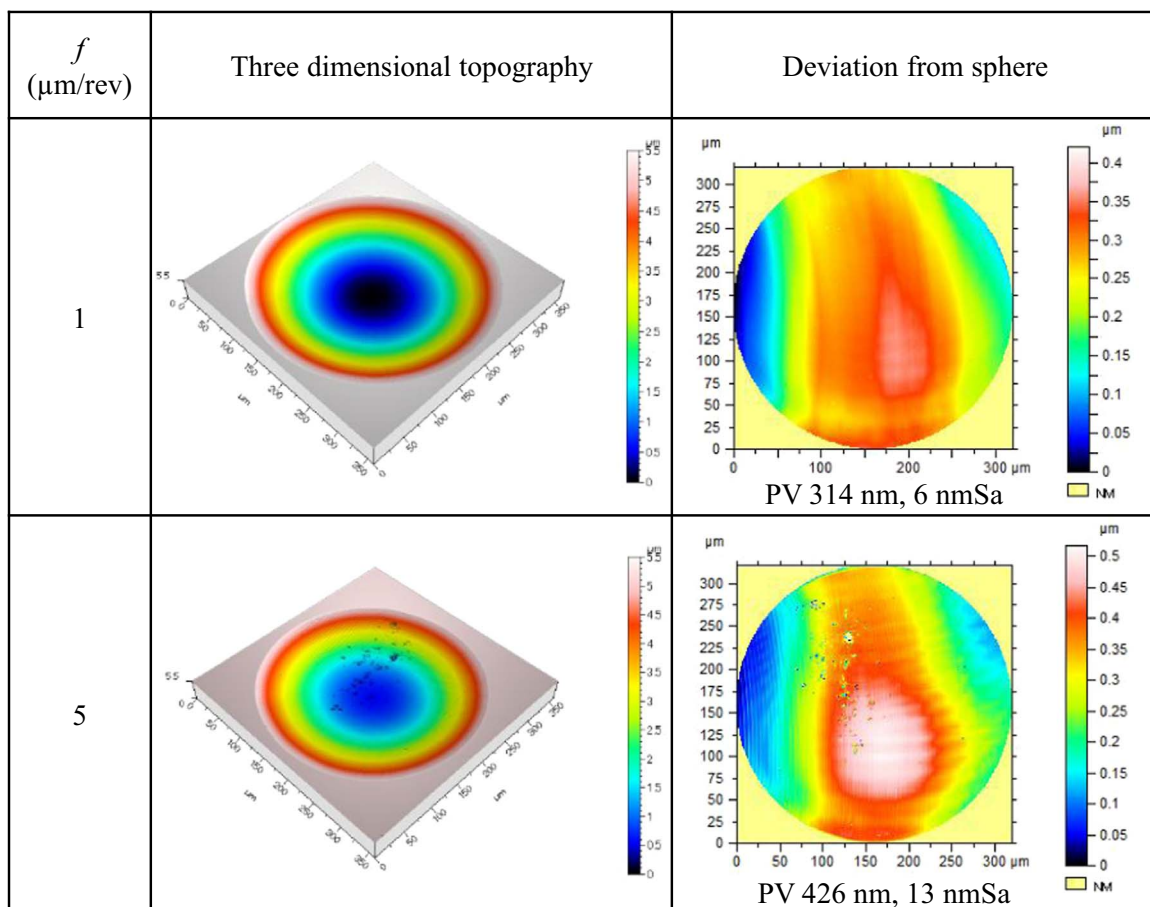


Fig. 6. Three-dimensional topographies of dimples located at $C = 0^\circ$, and their deviations from an ideal spherical surface.

single-crystal silicon wafer through ductile cutting in this experiment. The sample surfaces were then observed using a digital microscope. Fig. 4 shows microscope images of dimples located at $C=0^\circ$ and 45° , respectively, at different feed rates. When the cutting direction is along the $\langle 110 \rangle$ direction ($C=0^\circ$), brittle fractures (black dots) are found in the dimples at a feed rate over $5 \mu\text{m/rev}$. The results of dimples located at $C=90^\circ, 180^\circ, 270^\circ$ were similar to those at $C=0^\circ$ due to the crystalline symmetry. In contrast, brittle fractures are not observed in dimples located at $C=45^\circ, 135^\circ, 225^\circ, 315^\circ$ which had the cutting direction of $\langle 100 \rangle$ direction. This agrees with the previous results that the critical chip thickness of $\langle 110 \rangle$ direction is smaller than that of $\langle 100 \rangle$ direction when cutting single-crystal silicon (001) [33].

That is to say, the $\langle 100 \rangle$ direction is easier for ductile cutting than the $\langle 110 \rangle$ direction.

Fig. 5(a) shows SEM images of dimple surfaces located at $C=0^\circ$ machined at a feed rate of $1 \mu\text{m/rev}$. The surface is extremely smooth without any microcracks. At a feed rate of $5 \mu\text{m/rev}$, however, brittle fractures, the size of which is roughly $10 \mu\text{m}$, are formed on the dimple surface (Fig. 5(b)). In addition, it is seen in Fig. 4 that brittle fractures occurred preferentially at the left side of the dimples, while the right side is less damaged. The reason of this phenomenon will be discussed later in Section 3.7.

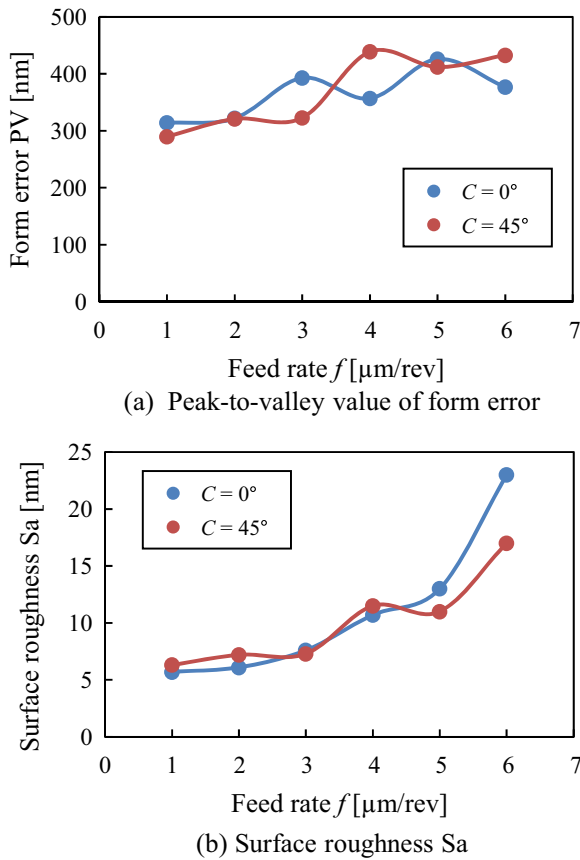


Fig. 7. Form error and surface roughness of dimples machined at different tool feed rates.

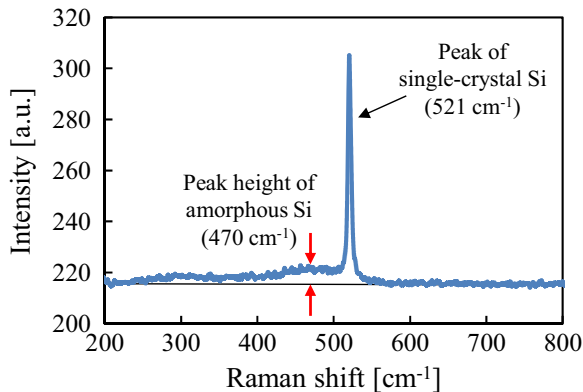


Fig. 8. A typical Raman spectrum showing a broadband peak of amorphous silicon in the center of the dimple machined at $C=45^\circ$ and $f=6 \mu\text{m}/\text{rev}$.

3.2. Surface topographical error

Next, the surfaces of the machined dimples were measured using a white light interferometer. Fig. 6 shows the three-dimensional topographies of the dimples machined at $C=0^\circ$ and $f=1$ and $5 \mu\text{m}/\text{rev}$. The deviation of a dimple surface from the ideal sphere ($R_d=2.563 \text{ mm}$) was calculated and shown in the same figure. From the deviation results, form error and surface roughness were further analyzed. Plots of form error and surface roughness of the dimples machined at various feed rates are shown in Fig. 7. It is seen that high-precision dimples with a form error of $\sim 300 \text{ nm}$ and surface roughness of $\sim 6 \text{ nmSa}$ were successfully obtained when a small tool feed rate ($< 2 \mu\text{m}/\text{rev}$) was used. As the feed rate increased, the form errors of the dimples increased slightly. Surface roughness increased corresponding to the

feed rate due to the occurrence of brittle fractures at high feed rates.

In general, the form error for an optical component is required to be less than $\lambda/4$, where λ is the wavelength of incident light [34]. Single-crystal silicon is an infrared optical material which has high transmittance in the wavelength range from 1.2 to $6 \mu\text{m}$. Thus, the form error of a silicon lens array should be less than 300 nm for $1.2 \mu\text{m}$ wavelength, and $1.5 \mu\text{m}$ for $6 \mu\text{m}$ wavelength, respectively. The present result has satisfied the form accuracy requirement over the entire infrared region for silicon.

Regarding surface roughness, the total integrated scattering (TIS) of an optical surface can be calculated by the following equation [35]:

$$\text{TIS} \approx \left(\frac{4\pi\delta}{\lambda} \right)^2 \quad (1)$$

where δ is the RMS surface roughness R_q . In general, TIS smaller than 1% is acceptable for most optical systems, thus surface roughness less than 10 nmRq is acceptable for $\lambda=1.2 \mu\text{m}$. R_q can be roughly estimated as 1.25 times R_a , thus surface roughness less than 8 nmR_a is required. The surface roughness achieved in the present study is 6 nmS_a , which has satisfied the highest requirements of surface roughness over the entire infrared region for silicon.

3.3. Material phase transformation

To investigate possible material structural changes of the machined dimples, laser micro-Raman spectroscopy was performed on the dimple surfaces. A typical Raman spectrum is shown in Fig. 8. Apart from a significant sharp peak at 521 cm^{-1} indicating single crystalline silicon, a broadband peak near 470 cm^{-1} is seen which demonstrates that silicon in the surface layer of the dimple has been partially transformed to amorphous. As known from previous studies, ductile mode cutting of single-crystal silicon is associated with phase transformation caused by high pressure [36]. The resulting amorphous silicon may affect the IR optical performances, such as refractive index, if it is very thick. For this reason, it is important to know how amorphous silicon is distributed within the micro dimples.

Fig. 9 shows mapping results of the peak heights for amorphous silicon for dimples machined under various conditions. The peak height was measured at 470 cm^{-1} from the base line of the Raman spectrum within the range between 200 cm^{-1} and 800 cm^{-1} , as shown in Fig. 8. It was found that the peak height of amorphous silicon increased as the feed rate increased. In addition, a higher amorphous peak seems to be located at the left side of the dimples. It should be pointed out that in Fig. 9, the tool feed direction is from the right to the left. Thus, amorphization of single-crystal silicon occurred preferentially at the exit side of tool feed of the lens dimple.

3.4. Chip formation

Fig. 10 shows SEM images of cutting chips obtained under different conditions. Continuous chips, which indicate ductile cutting mode, were generated at $f=1 \mu\text{m}/\text{rev}$ (Fig. 10(a)) for a $5 \mu\text{m}$ -deep lens dimple. The chips are not very long, because cutting was interrupted by separated dimples. On the other hand, a mixture of powder chips and a few continuous chips were found at $f=6 \mu\text{m}/\text{rev}$ (Fig. 10(b)). This means that both brittle and ductile cutting modes existed under this condition, which agrees with the surface observation results in Fig. 4. Fig. 10(c) is an SEM image of cutting chips obtained at $f=1 \mu\text{m}/\text{rev}$ when cutting a shallower lens array (lens depth $D=2 \mu\text{m}$). In this case, the chips look much thinner and longer than those in Fig. 10(a) where the lens depth is $5 \mu\text{m}$, and some chips are even partially transparent. When the lens depth is $2 \mu\text{m}$, the maximum undeformed chip thickness is extremely small (68 nm), enabling this kind of extremely thin chip formation.

Laser micro-Raman spectroscopy was also performed to detect the

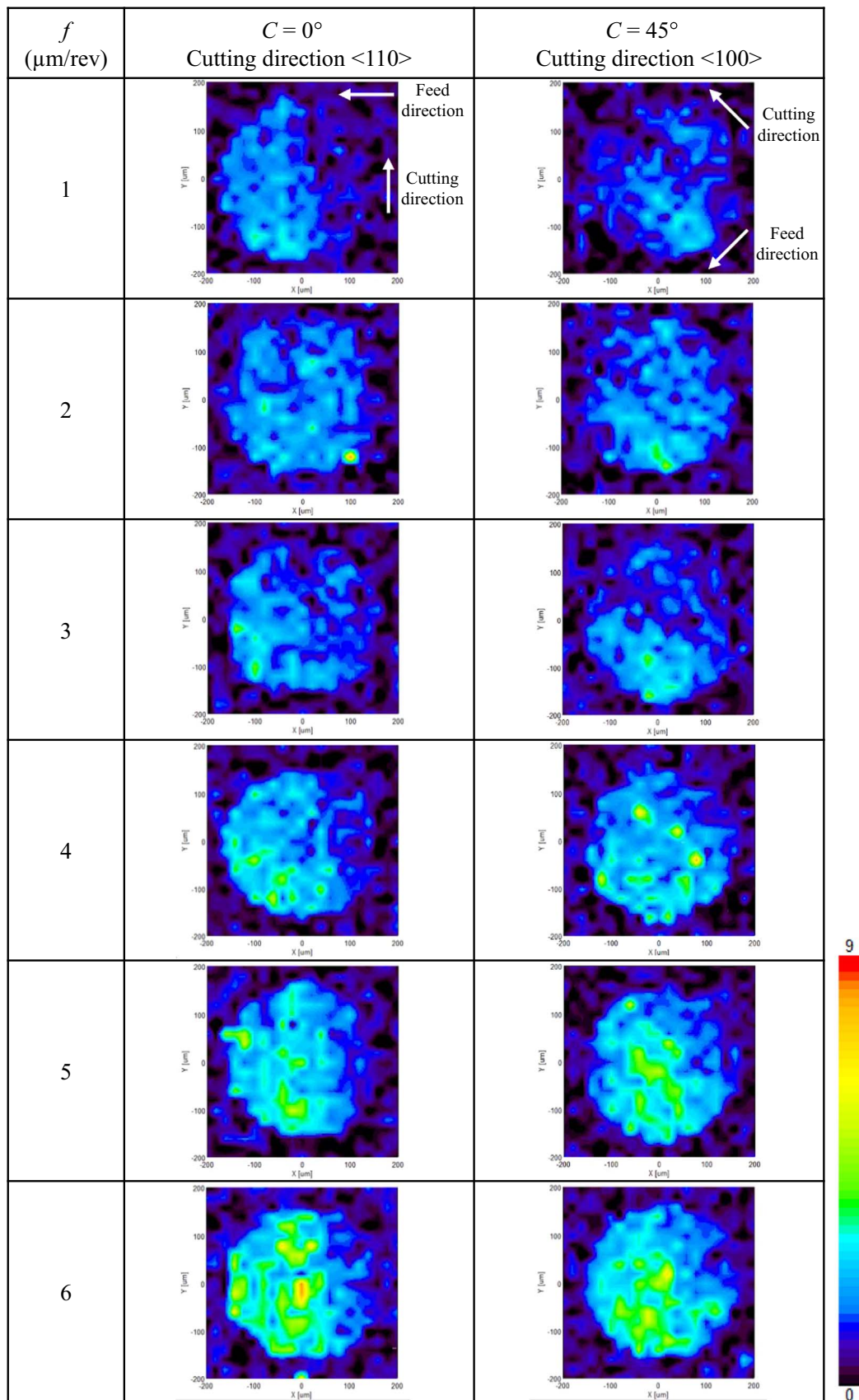
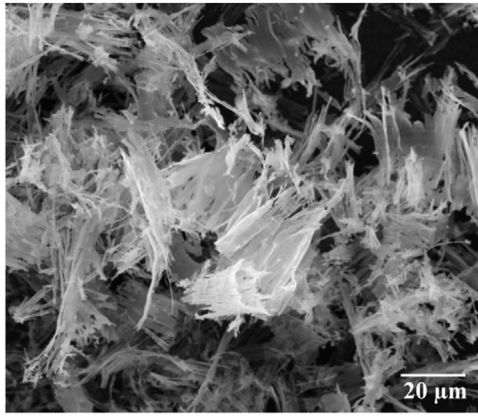
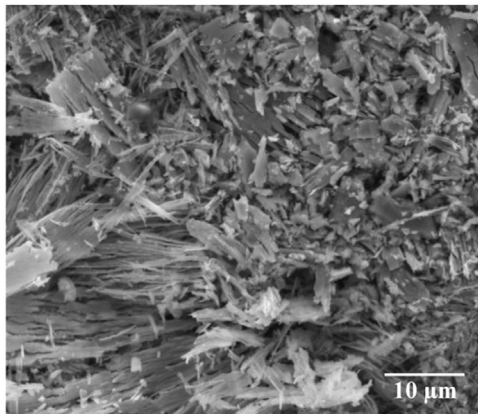


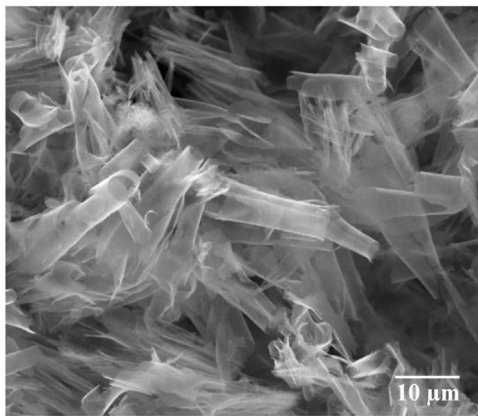
Fig. 9. Mapping results of peak height of amorphous silicon measured using a laser micro-Raman spectrometer.



(a) $D = 5 \mu\text{m}, f = 1 \mu\text{m/rev}$



(b) $D = 5 \mu\text{m}, f = 6 \mu\text{m/rev}$



(c) $D = 2 \mu\text{m}, f = 1 \mu\text{m/rev}$

Fig. 10. SEM images of chips obtained when cutting lens dimples with different depths at different tool feed rates.

microstructure of cutting chips. Fig. 11 shows the Raman spectrum of chips obtained at $f=1$ and $6 \mu\text{m/rev}$. In case of $f=1 \mu\text{m/rev}$, some areas of chips only showed the peak of amorphous silicon (Fig. 11(a)), and other areas showed a mixture of amorphous silicon and polycrystalline silicon (Fig. 11(b)). This fact agrees with previous results where amorphous and poly-crystalline chips are generated in ductile cutting [36]. On the other hand, in case of $f=6 \mu\text{m/rev}$ only peak of polycrystalline silicon was detected (Fig. 11(c)). This indicates that in brittle cutting mode, phase transformation to amorphous silicon did not occur.

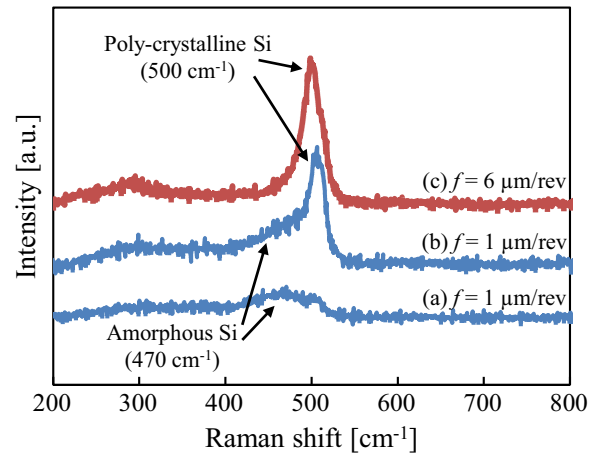
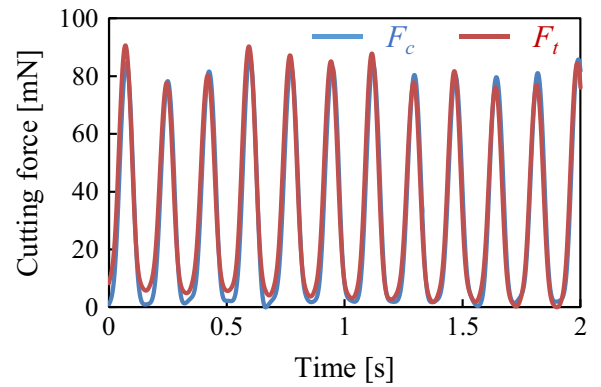
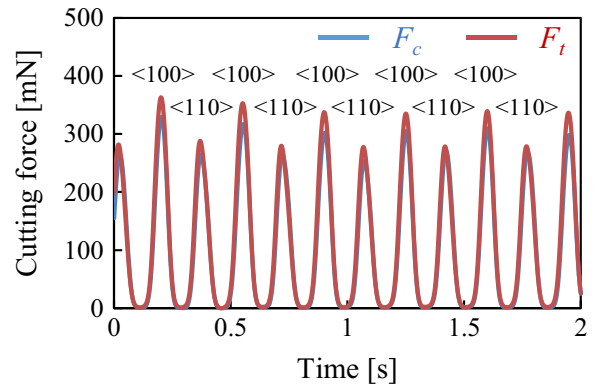


Fig. 11. Raman spectra of cutting chips showing different significance for amorphous and poly-crystalline phases.



(a) $f = 1 \mu\text{m/rev}$



(b) $f = 5 \mu\text{m/rev}$

Fig. 12. Variations of cutting forces at different tool feed rates. A strong dependence of peak force on crystal orientation is seen at high tool feed rates.

3.5. Cutting force characteristics

Cutting force was measured during lens array cutting. A low pass filter was applied to remove noise caused by power source. Principal force F_c and thrust force F_t was evaluated in detail, while feed force F_f was distinctly smaller compared to F_c and F_t , and thus neglected in this experiment. Fig. 12 shows the force waviness of F_c and F_t in case of $f=1$ and $5 \mu\text{m/rev}$, respectively, where the force waviness was recorded when the tool passed the center of dimples ($X=1 \text{ mm}$). Both F_c and F_t change periodically because the depth of cut changes during cutting dimples. It was found that the peak value of cutting force was almost

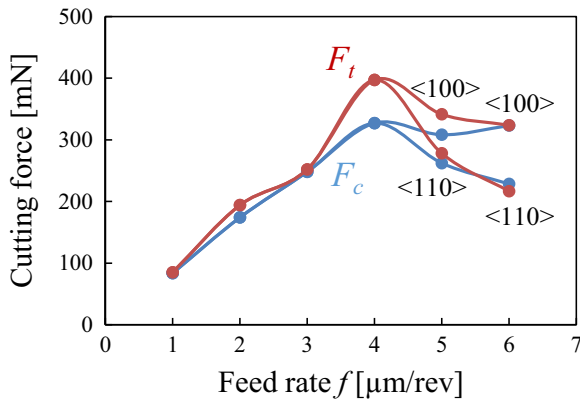


Fig. 13. Relationship between cutting forces and tool feed rate.

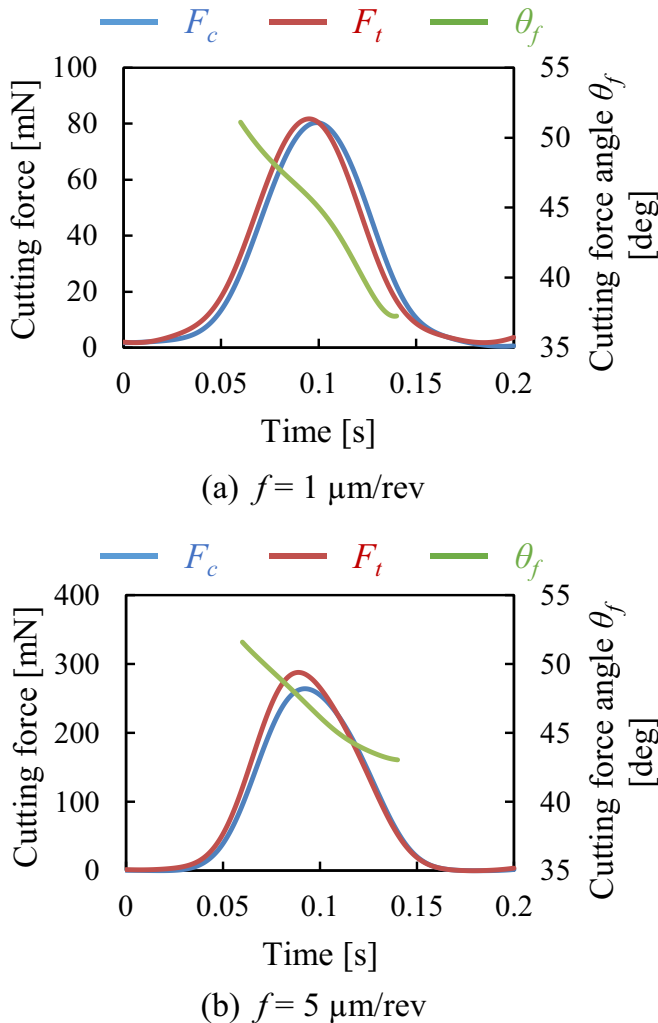
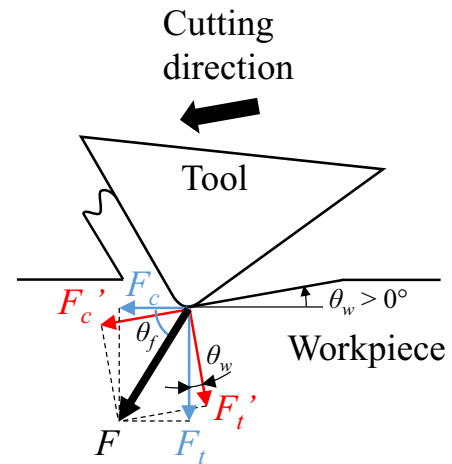


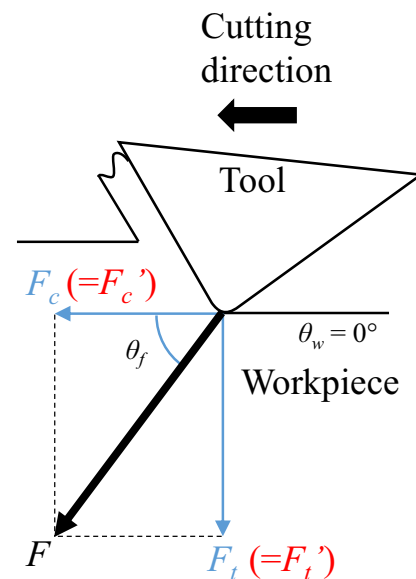
Fig. 14. Variation of cutting force and cutting force angle during cutting a single dimple.

the same for various crystal orientations at $f=1 \mu\text{m/rev}$ (Fig. 12(a)), while it changed greatly depending on crystal orientation at $f=5 \mu\text{m/rev}$ (Fig. 12(b)). A smaller peak force corresponds to the $\langle 110 \rangle$ direction where brittle fractures occur, while a larger peak force corresponds to the $\langle 100 \rangle$ direction where ductile cutting is dominant, as shown in Fig. 4.

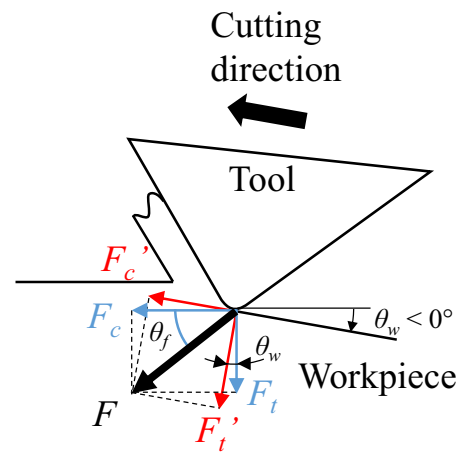
The average peak values of cutting forces at various feed rates are plotted in Fig. 13. In case of $f=5, 6 \mu\text{m/rev}$, the average values of low peaks and high peaks were plotted separately with respect to crystal orientations. It is found that cutting forces increase as the feed rate



(a) Beginning of cutting



(b) At the bottom of a dimple



(c) End of cutting

Fig. 15. Change in cutting force angle when cutting a single dimple.

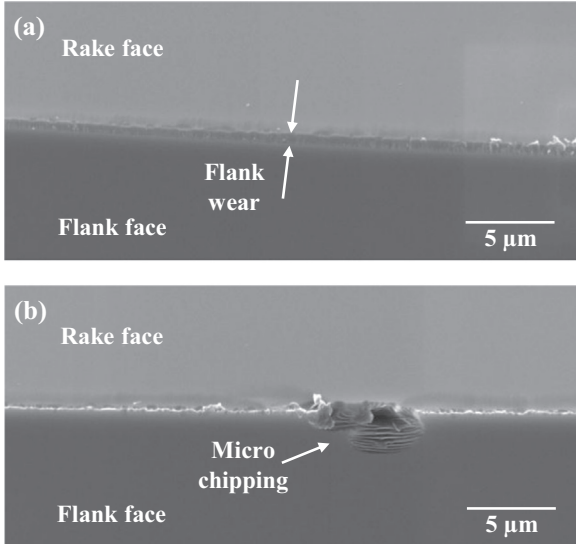


Fig. 16. SEM images of tool edge after dimple cutting on single-crystal silicon, showing two kinds of wear patterns: (a) flank wear and (b) micro chipping.

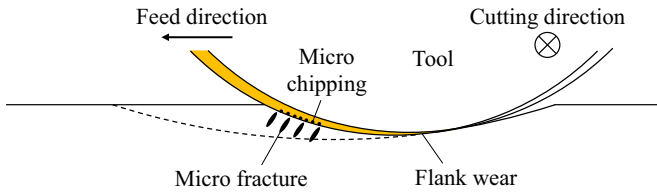


Fig. 17. Schematic diagram for two kinds of tool wear patterns in dimple cutting.

increases when $f < 5 \mu\text{m}/\text{rev}$, and decrease when $f > 5 \mu\text{m}/\text{rev}$. This drop of force corresponds to the occurrence of brittle fractures as shown in Fig. 4. The stiffness of the machine tool used in this study is $2.1 \times 10^8 \text{ N/m}$. Thus, the displacement of the tool tip induced by a thrust force of $F_t = 400 \text{ mN}$ is less than 2 nm. Such a displacement is vanishingly small compared to the total form error of the lens ($\sim 300 \text{ nm}$).

It was also found that during cutting a single dimple, F_t reached its maximum earlier than F_c , as shown in Fig. 14. This phenomenon was also observed in previous research on dimple-cutting by elliptical vibration texturing on a ductile material [37]. In this paper, cutting force angle θ_f is defined in Fig. 15, which can be calculated by the following equation:

$$\theta_f = \tan^{-1} \frac{F_t}{F_c} \quad (2)$$

The changes of cutting force angle θ_f are additionally plotted in Fig. 14. It is clear that in Fig. 14(a) and (b), θ_f decreases during the cutting of a single dimple.

Fig. 15 shows schematically the decomposition of a cutting force at different stages when cutting a single dimple. When start cutting a dimple, the tool moves into the workpiece inducing a positive cutting direction angle θ_w , as shown in Fig. 15(a). As the tool reaches the deepest point of a dimple, θ_w decreases to zero (Fig. 15(b)), and then θ_w becomes negative as the tool moves away from the workpiece (Fig. 15(c)). In the present study, the dynamometer measures the force components parallel (F_c) and vertical (F_t) to the flat surface of the workpiece. However, the actual principal force F_c' and thrust force F_t' are parallel and vertical to the cutting direction, as described in Fig. 15. Then the cutting force angle θ_f can be calculated as follows:

$$\theta_f = \theta_w + \tan^{-1} \frac{F_t'}{F_c'} \quad (3)$$

Therefore, θ_f changes with θ_w . In the present experiment, θ_w

changed from 3.58° to -3.58° , thus θ_f should be decreased by about 7° during cutting a single dimple. This result agrees very well with the experimental results in Fig. 14.

3.6. Tool wear characteristics

The diamond tool was observed using SEM after cutting dimples with a total cutting distance of 500 mm. Fig. 16 shows SEM images of the tool edge. Two kinds of tool wear patterns were identified: one is flank wear (wear land width $\sim 700 \text{ nm}$) near the tool apex (Fig. 16(a)); the other is micro chippings near the region contacting with the uncut surface (Fig. 16(b)). As shown in Fig. 17, undeformed chip thickness is extremely small and approaches zero near the tool apex, where intensive friction between the tool and the workpiece causes flank wear. Near the region contacting with the uncut surface, however, undeformed chip thickness is very large, thus brittle mode cutting leads to micro impacts to the tool, causing micro chippings to happen [38].

In the microscope images of Fig. 4, it is noteworthy that the left sides of the dimples look rougher than the right side for both $\langle 110 \rangle$ and $\langle 100 \rangle$ directions at high feed rate ($f > 4 \mu\text{m}/\text{rev}$). This surface feature may be due to the tool wear. Fig. 18 shows surface topographies of dimples machined at $f = 5 \mu\text{m}/\text{rev}$ for both $C = 0^\circ$ and 45° , and the results of surface roughness measurements over a $70 \mu\text{m}$ square at each side of the dimples. It is evident that the surface roughness of the left side is worse than that of the right side. The micro chippings occurred to the left side of the tool are transferred to the finished surface and resulted in larger surface roughness.

3.7. Discussion on material removal mechanism

In microlens array cutting, depth of cut constantly changes with time and location, leading to changes of undeformed chip thickness. Fig. 19 shows a schematic model for undeformed chip thickness when cutting a spherical dimple using a round-nosed tool, where R_d is the curvature radius of the dimple, O_d the projected center of the dimple curvature, R_t the nose radius of the tool, D the depth of the dimple, f the tool feed rate. The previous and the current tool path are described as circular arcs of which O_{t0} and O_{t1} are the centers, respectively. When the distance between the center of workpiece and the tool tip of the current path is $X_{O_{t1}}$, the maximum undeformed chip thickness h_{max} and the location $X_{h_{max}}$ where undeformed chip thickness becomes a maximum are calculated as follows:

$$\theta_1 = \sin^{-1} \left(\frac{X_{O_{t1}}}{R_d - R_t} \right) \quad (4)$$

$$\theta_0 = \sin^{-1} \left(\frac{X_{O_{t1}} + f}{R_d - R_t} \right) \quad (5)$$

$$\Delta Z = (R_d - R_t)(\cos \theta_1 - \cos \theta_0) \quad (6)$$

$$d_1 = (R_d - R_t) \cos \theta_1 + R_t - R_d + D \quad (7)$$

$$d_0 = d_1 - \Delta Z \quad (8)$$

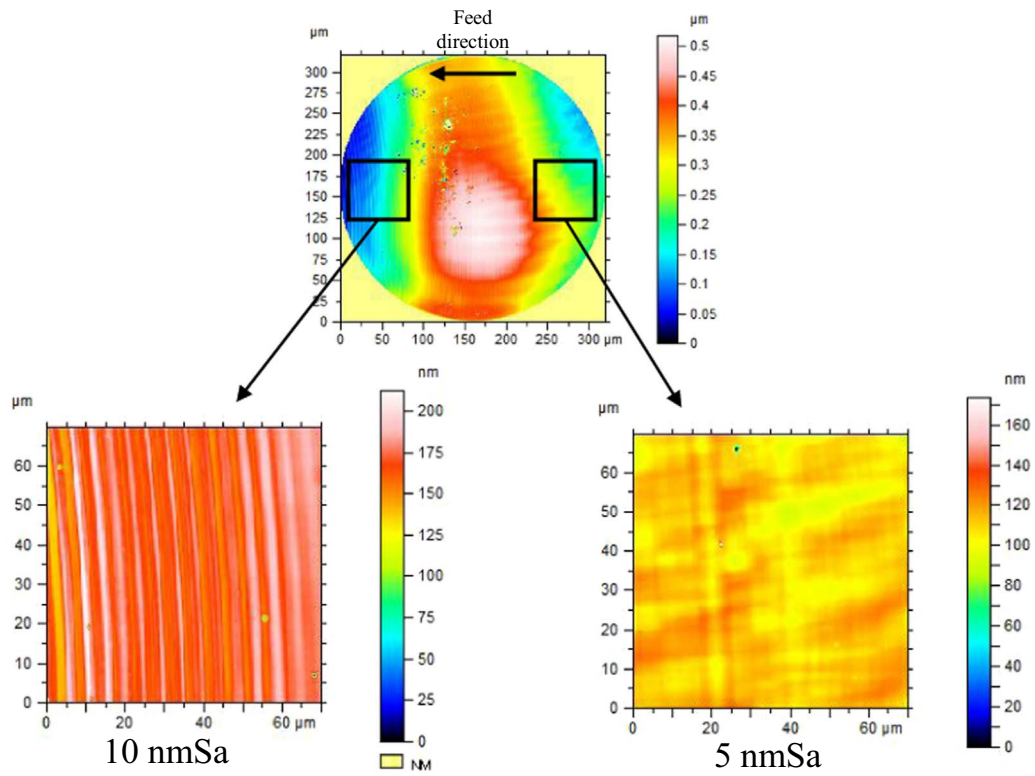
$$x = \sqrt{R_t^2 - (R_t - d_0)^2} - f \quad (9)$$

$$h_{max} = R_t - \sqrt{x^2 + (R_t - d_1)^2} \quad (10)$$

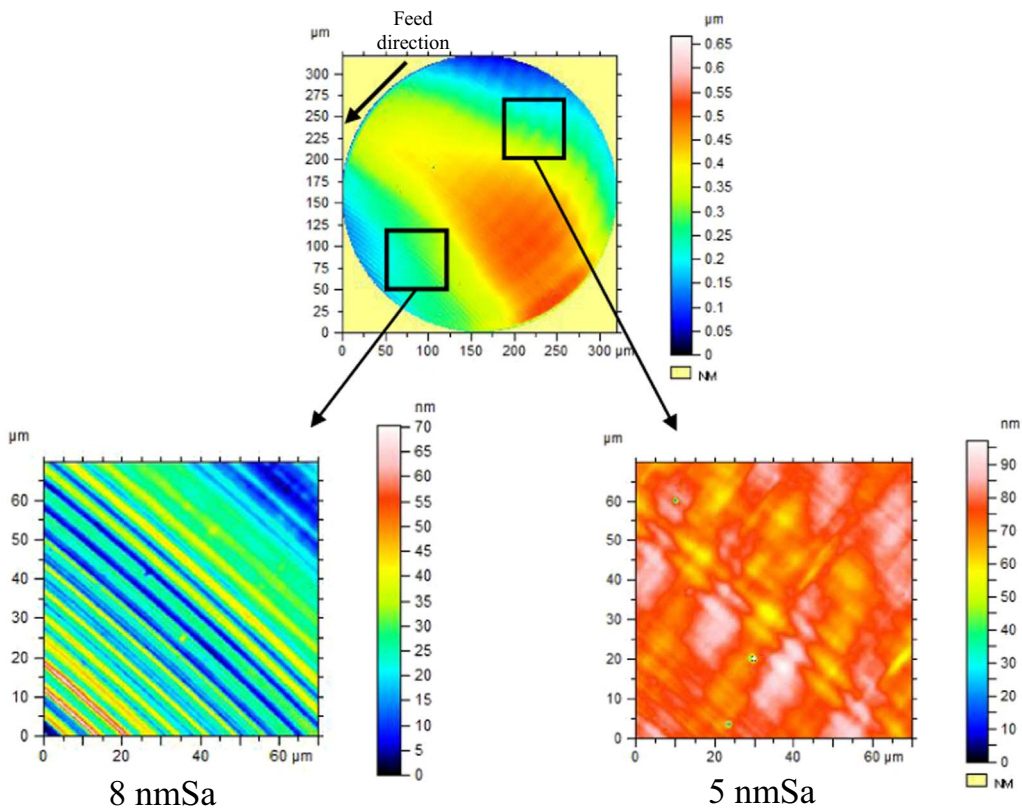
$$\theta_{h_{max}} = \tan^{-1} \left(\frac{x}{R_t - d_1} \right) \quad (11)$$

$$X_{h_{max}} = (R_d - R_t) \sin \theta_1 - R_t \sin \theta_{h_{max}} \quad (12)$$

In addition, if undeformed chip thickness is given as h_θ , the distance X_{h_θ} and the depth d_{h_θ} in Fig. 19(b) can be calculated as follows:



(a) $f = 5 \mu\text{m/rev}$, $C = 0^\circ$



(b) $f = 5 \mu\text{m/rev}$, $C = 45^\circ$

Fig. 18. Surface roughness change within a single dimple caused by tool wear.

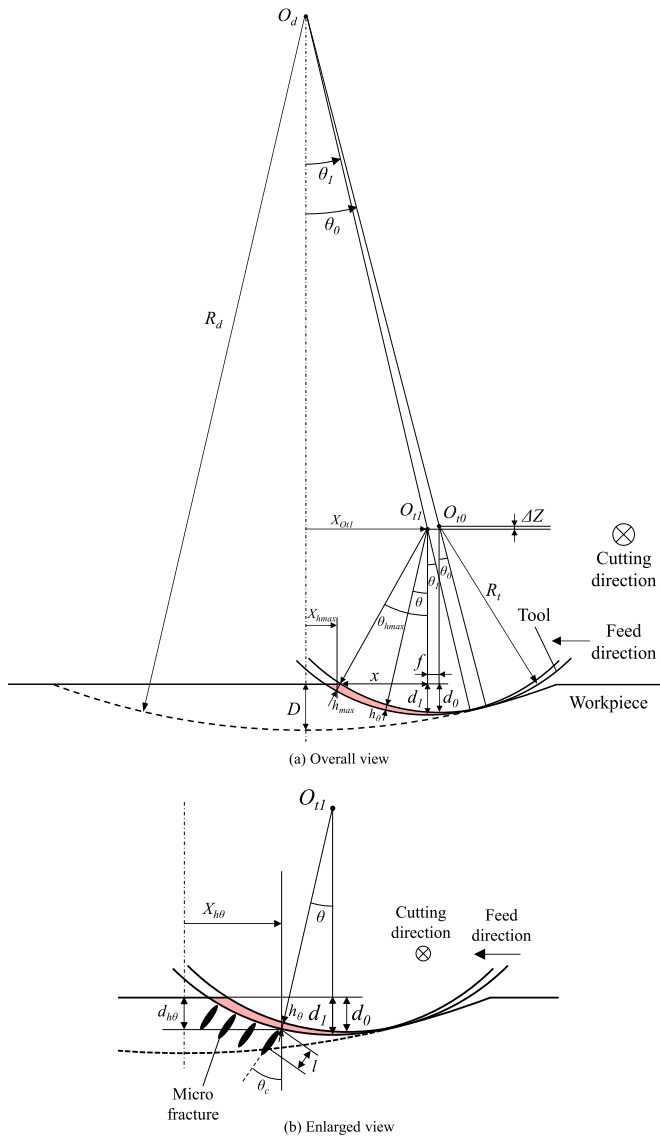


Fig. 19. Schematic models for calculating undeformed chip thickness in spherical dimple cutting.

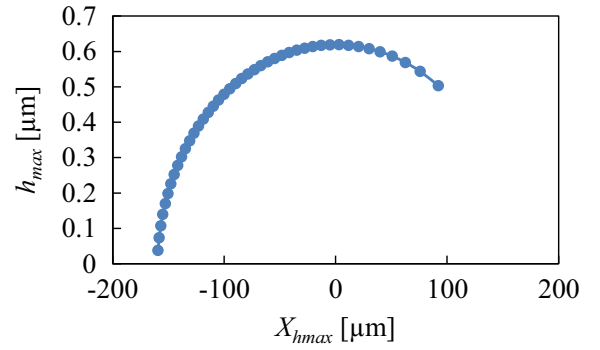
$$\theta = \cos^{-1} \left(\frac{-R_t^2 + (R_t - h_\theta)^2 + f^2 + (\Delta Z)^2}{2(R_t - h_\theta) \sqrt{f^2 + (\Delta Z)^2}} \right) - \frac{\pi}{2} - \tan^{-1} \frac{\Delta Z}{f} \quad (13)$$

$$X_{h\theta} = (R_d - R_t) \sin \theta_1 - R_t \sin \theta \quad (14)$$

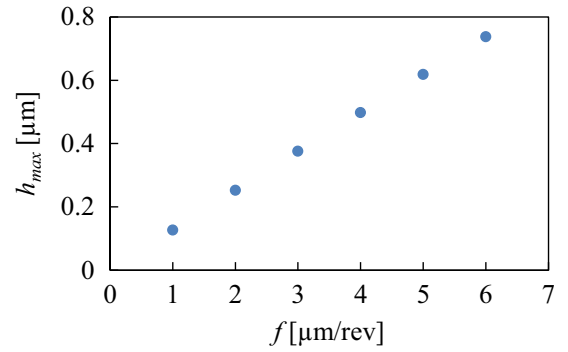
$$d_{h\theta} = (R_d - R_t) \cos \theta_1 + R_t \cos \theta - R_d + D \quad (15)$$

Then h_{max} and $X_{h_{max}}$ were calculated using experimental parameters of the present study. Fig. 20(a) shows the relationship between h_{max} and $X_{h_{max}}$ in case of $f = 5 \mu\text{m/rev}$. It was found that h_{max} changed symmetrically with respect to the center of the dimple. This symmetric change was not dependent on R_d , R_t , f and D . Fig. 20(b) shows the maximum value of h_{max} at each feed rate, which increased linearly. Fig. 20(c) shows the relationship between $X_{h\theta}$ and $d_{h\theta}$ where h_θ is set to 400 nm as an example. In this case, $d_{h\theta}$ changed symmetrically too with respect to the center of the dimple.

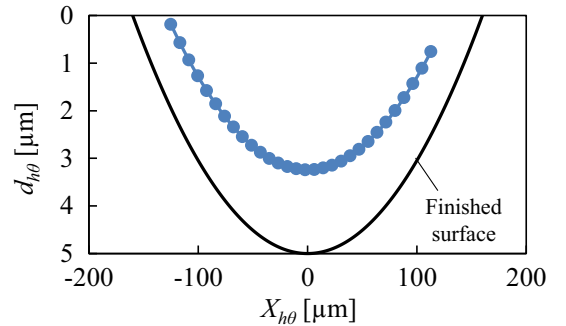
The tendency that brittle fractures occurred preferentially at the left sides of the dimples can be explained from the viewpoint of cleavage plane orientation. Normally cracks are generated along cleavage planes when undeformed chip thickness is larger than a critical value, and cracks penetrate in the direction of cleavage plane θ_c as shown in Fig. 19(b). The cleavage plane of single-crystal silicon is (111), and the angle between (001) and (111) is 54.7° , as shown in Fig. 21. Thus



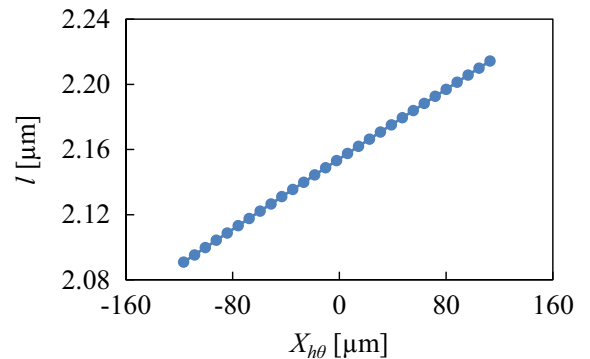
(a) Distribution of maximum undeformed chip thickness at $f = 5 \mu\text{m/rev}$



(b) Maximum value of h_{max} at each feed rate



(c) Distribution of the point at which undeformed chip thickness is 400 μm at $f = 5 \mu\text{m/rev}$



(d) Length to the finished surface at an angle of $\theta_c = 35.3^\circ$ at $f = 5 \mu\text{m/rev}$

Fig. 20. Calculation results of undeformed chip thickness under various conditions.

$\theta_c = 35.3^\circ$ when the cutting direction is $\langle 110 \rangle$. If the length l in Fig. 19(b) is shorter than the crack length, cracks will remain on the finished surface. Here, l can be calculated as follows:

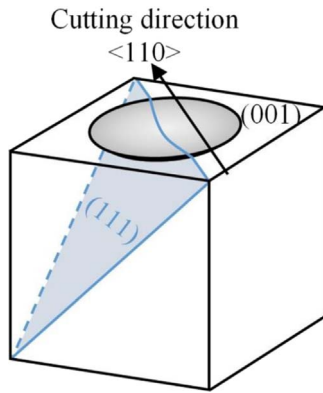


Fig. 21. Schematic of the relationship between a dimple surface and a cleavage plane.

$$Z_{h\theta} = (R_d - R_t) \cos \theta_l + R_t \cos \theta \quad (16)$$

$$l = -(Z_{h\theta} \cos \theta_c - X_{h\theta} \sin \theta_c) + \sqrt{(Z_{h\theta} \cos \theta_c - X_{h\theta} \sin \theta_c)^2 - Z_{h\theta}^2 - X_{h\theta}^2 + R_d^2} \quad (17)$$

Fig. 20(d) shows the relationship between $X_{h\theta}$ and l when h_θ is 400 nm and $f=5 \mu\text{m}/\text{rev}$. It is found that l decreased as $X_{h\theta}$ decreased, which means cracks reach the finished surface more easily at the left side of the dimples. For example, supposing that cracks are generated when h_θ is over 400 nm and the crack length is $2.15 \mu\text{m}$, cracks generated from the point where $X_{h\theta}$ is from $-117 \mu\text{m}$ to $-10 \mu\text{m}$ will remain on the finished surface. This situation agrees well with the microscopic observation results of Fig. 4.

4. Conclusions

Micro-lens arrays have been machined on single-crystal silicon (001) by STS diamond turning under various conditions. The dimple form error, surface topography, material phase transformation, cutting force characteristics were evaluated. The following conclusions are obtained:

- (1) Brittle fracture occurs on the dimple surface when cutting direction is $\langle 110 \rangle$ and tool feed rate is higher than $5 \mu\text{m}/\text{rev}$. Cracks occur preferentially at one side (the exit side of tool feed) of the dimple.
- (2) Amorphous silicon phase is generated significantly at one side (the exit side of tool feed) of the dimple as tool feed rate increases.
- (3) Cutting force increases as the feed rate increases, and then decreases as the feed rate increases further due to the occurrence of brittle fractures.
- (4) The peak cutting forces at various cutting directions were different at high tool feed rates, which is caused by crystal anisotropy.
- (5) When cutting a single dimple, cutting force angle always changes. The thrust force reaches its maximum earlier than the principle force.
- (6) Two kinds of tool wear patterns were observed. One is micro chippings near the region contacting with the uncut surface where brittle mode cutting takes place; the other is flank wear near the tool apex where ductile cutting is dominant. The micro chippings affect surface roughness distribution inside a dimple.
- (7) Spherical micro-lens arrays with a form error of $\sim 300 \text{ nmPV}$ and surface roughness of $\sim 6 \text{ nmSa}$ were successfully fabricated.

Acknowledgements

The authors would like to extend their thanks to AMETEK Precitech Inc., USA, for providing technical supports of the ultraprecision diamond turning lathe used in this study.

References

- [1] A.R. Abdul Manaf, J. Yan, Press molding of a Si-HDPE hybrid lens substrate and evaluation of its infrared optical properties, *Precis. Eng.* 43 (2016) 429–438.
- [2] K. Morishita, K. Nakajima, T. Fujii, M. Shiinoki, Near-net shaping of single-crystal silicon for optical lens by one-shot pressing at temperature just below silicon melting point and its demonstration of optical properties, *Appl. Phys. Express* 4 (2011) 106501.
- [3] W. Kim, H. Matsuhara, T. Onaka, H. Kataya, T. Wada, K. Uemizu, M. Ueno, H. Murakami, N. Fujishiro, D. Ishihara, H. Watarai, W. Takeyama, Y. Ikeda, Optical performance evaluation of Near infrared camera (NIR) on board ASTRO-F, *Proc. SPIE* 5904 (2005) 590418.
- [4] D.A. Fletcher, K.B. Crozier, C.F. Quate, G.S. Kino, K.E. Goodson, Near-field infrared imaging with a microfabricated solid immersion lens, *Appl. Phys. Lett.* 77 (14) (2000) 2109–2111.
- [5] Z. Deng, Q. Yang, F. Chen, X. Meng, H. Bian, J. Yong, C. Shan, X. Hou, Fabrication of large-area concave microlens array on silicon by femtosecond laser micro-machining, *Opt. Lett.* 40 (9) (2015) 1928–1931.
- [6] R. Bitterli, T. Scharf, H.P. Herzig, W. Noell, N. Rooij, A. Bich, S. Roth, K.J. Weible, R. Voelkel, M. Zimmermann, M. Schmidt, Fabrication and characterization of linear diffusers based on concave micro lens arrays, *Opt. Express* 18 (13) (2010) 14251–14261.
- [7] Z. Deng, Q. Yang, F. Chen, H. Bian, J. Yong, G. Du, Y. Hu, X. Hou, High-performance laser beam homogenizer based on double-sided concave microlens, *IEEE Photonics Technol. Lett.* 26 (20) (2014) 2086–2089.
- [8] G. Molar-Velázquez, F.J. Renero-Carrillo, W. Calleja-Arriaga, Two-dimensional optical micro-scanner on silicon technology, *Optik* 121 (2010) 843–846.
- [9] Y.Z. Wang, D.H. Li, C.G. Luo, Q.H. Wang, Viewing angle enhanced integral imaging display based on double-micro-lens array, *J. Soc. Inf. Disp.* 21 (7) (2013) 289–294.
- [10] W. Xie, Q.H. Wang, Y.Z. Wang, H. Deng, Depth-enhanced integral imaging system with convex and composite concave micro-lens arrays, *Optik* 125 (2014) 6087–6089.
- [11] C.Y. Chang, S.Y. Yang, L.S. Huang, J.H. Chang, Fabrication of plastic microlens array using gas-assisted micro-hot-embossing with a silicon mold, *Infrared Phys. Technol.* 48 (2006) 163–173.
- [12] J. Albero, L. Nieradko, C. Gorecki, H. Ottevaere, V. Gomez, H. Thienpont, J. Pietarinen, B. Päivänranta, N. Passilly, Fabrication of spherical microlenses by a combination of isotropic wet etching of silicon and molding techniques, *Opt. Express* 17 (8) (2009) 6283–6292.
- [13] O.G. Oliveira, D.W. Lima Monteiro, R.F.O. Costa, Optimized microlens-array geometry for Hartmann-Shack wavefront sensor, *Opt. Laser Eng.* 55 (2014) 155–161.
- [14] P. He, L. Li, H. Li, J. Yu, L. James Lee, A.Y. Yi, Compression molding of glass freeform optics using diamond machined silicon mold, *Manuf. Lett.* 2 (2014) 17–20.
- [15] Y.S. Ow, M.B.H. Breese, S. Azimi, Fabrication of concave silicon micro-mirrors, *Opt. Express* 18 (14) (2010) 14511–14518.
- [16] A. Pan, B. Gao, T. Chen, J. Si, C. Li, F. Chen, X. Hou, Fabrication of concave spherical microlenses on silicon by femtosecond laser irradiation and mixed acid etching, *Opt. Express* 22 (12) (2014) 15245–15250.
- [17] P.N. Blake, R.O. Scattergood, Ductile-regime machining of germanium and silicon, *J. Am. Ceram. Soc.* 73 (4) (1990) 949–957.
- [18] T. Nakasui, S. Kodera, S. Hara, H. Matsunaga, N. Ikawa, S. Shimada, Diamond turning of brittle materials for optical components, *Ann. CIRP* 39 (1) (1990) 89–92.
- [19] T. Shibata, S. Fujii, E. Makino, M. Ikeda, Ductile-regime turning mechanism of single-crystal silicon, *Precis. Eng.* 18 (1996) 129–137.
- [20] J. Yan, M. Yoshino, T. Kuriyagawa, T. Shirakashi, K. Syoji, R. Komanduri, On the ductile machining of silicon for micro electro-mechanical systems (MEMS), optoelectronic and optical applications, *Mat. Sci. Eng. A* 297 (2001) 230–234.
- [21] J. Yan, K. Syoji, T. Kuriyagawa, H. Suzuki, Ductile regime turning at large tool feed, *J. Mater. Process Tech.* 121 (2002) 363–372.
- [22] J. Yan, J. Tamaki, K. Syoji, T. Kuriyagawa, Development of a novel ductile-machining system for fabricating axisymmetric aspheric surfaces on brittle materials, *Key Eng. Mat.* 238–239 (2003) 43–48.
- [23] K. Liu, X.P. Li, M. Rahman, K.S. Neo, X.D. Liu, A study of the effect of tool cutting edge radius on ductile cutting of silicon wafers, *Int. J. Adv. Manuf. Technol.* 32 (2007) 631–637.
- [24] R.G. Jasinevicius, J.G. Duduch, L. Montanari, P.S. Pizani, Dependence of brittle-to-ductile transition on crystallographic direction in diamond turning of single-crystal silicon, *Proc. Inst. Mech. Eng. B-J. Eng.* 226 (2012) 445–458.
- [25] A.Y. Yi, L. Li, Design and fabrication of a microlens array by use of a slow tool servo, *Opt. Lett.* 30 (13) (2005) 1707–1709.
- [26] F.Z. Fang, X.D. Zhang, X.T. Hu, Cylindrical coordinate machining of optical freeform surfaces, *Opt. Express* 16 (10) (2008) 7323–7329.
- [27] G.E. Davis, J.W. Roblee, A.R. Hedegs, Comparison of freeform manufacturing techniques in the production of monolithic lens arrays, *Proc. SPIE* 7426 (2009) 726505.
- [28] S. Scheiding, A.Y. Yi, A. Gebhardt, R. Loose, L. Li, S. Risse, R. Eberhardt, A. Tünnermann, Diamond milling or turning for the fabrication of micro lens arrays: comparing different diamond machining technologies, *Proc. SPIE* 7927 (2011) 79270N.
- [29] L.B. Kong, C.F. Cheung, Design, fabrication and measurement of ultra-precision micro-structured freeform surfaces, *Comput. Ind. Eng.* 61 (2011) 216–225.
- [30] D.P. Yu, G.S. Hong, Y.S. Wong, Profile error compensation in fast tool servo diamond turning of micro-structured surfaces, *Int. J. Mach. Tools Manuf.* 52

- (2012) 13–23.
- [31] X. Zhang, F. Fang, L.H. Yu, L. Jiang, Y. Guo, Slow slide servo turning of compound eye lens, *Opt. Eng.* 52 (2) (2013) 023401.
- [32] D.P. Yu, Y.S. Wong, G.S. Hong, Ultraprecision machining of micro-structured functional surfaces on brittle materials, *J. Micro. Micro.* 21 (2011) 095011.
- [33] J. Yan, T. Asami, H. Harada, T. Kuriyagawa, Crystallographic effect on subsurface damage formation in silicon microcutting, *CIRP Ann.* 61 (2012) 131–134.
- [34] H. Ottevaere, R. Cox, H.P. Herzig, T. Miyashita, K. Naessens, M. Taghizadeh, R. Völkel, H.J. Woo, H. Thienpont, Comparing glass and plastic refractive microlenses fabricated with different technologies, *J. Opt. A-Pure Appl. Opt.* 8 (2006) S407–S429.
- [35] J.E. Harvey, S. Schröder, N. Choi, A. Duparré, Total integrated scatter from surfaces with arbitrary roughness, correlation widths, and incident angles, *Opt. Eng.* 51 (1) (2012) 013402.
- [36] J. Yan, T. Asami, H. Harada, T. Kuriyagawa, Fundamental investigation of subsurface damage in single crystalline silicon caused by diamond machining, *Precis. Eng.* 33 (2009) 378–386.
- [37] R. Kurniawan, G. Kiswanto, T.J. Ko, Micro-dimple pattern process and orthogonal cutting force analysis of elliptical vibration texturing, *Int. J. Mach. Tools Manuf.* 106 (2016) 127–140.
- [38] J. Yan, K. Syoji, J. Tamaki, Some observations on the wear of diamond tools in ultra-precision cutting of single-crystal silicon, *Wear* 255 (2003) 1380–1387.